Materials & Design 209 (2021) 109949

Contents lists available at ScienceDirect

Materials & Design

journal homepage: www.elsevier.com/locate/matdes

Synthesis and electrochemical properties of nanoporous CrN thin film electrodes for supercapacitor applications

Zecui Gao [a,b], Zhixin Wan [c], Zhengtao Wu [a], Xueli Huang [a], Haiqing Li [a], Teng Fei Zhang [a,*], Paul Heinz Mayrhofer [b], Qimin Wang [a,*]

[a] School of Electromechanical Engineering, Guangdong University of Technology, Guangzhou 510006, China
[b] Institute of Materials Science and Technology, Technische Universität Wien, Getreidemarkt 9, 1060 Vienna, Austria
[c] School of Materials Science & Engineering, Sun Yat-sen University, Guangzhou 510006, China

HIGHLIGHTS

- Sufficient Ni content leads to an interconnected Ni-network in the CrN–Ni coating.
- Nanoporous CrN can be obtained by HCl etching of CrN–Ni.
- Nanoporous CrN has an ~ 80% higher specific capacitance than CrN.
- Guideline to prepare porous transition metal nitrides with a high specific surface area.

GRAPHICAL ABSTRACT

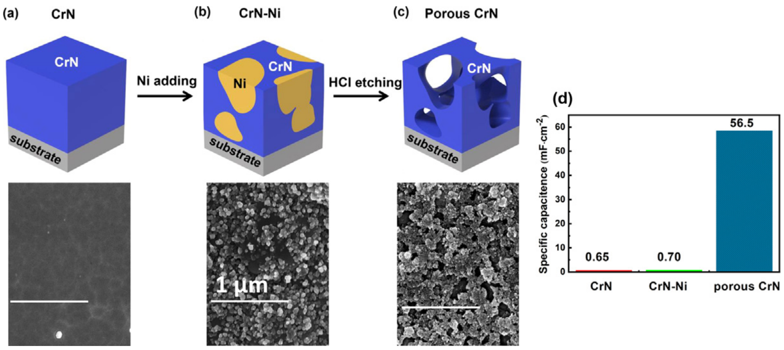

ARTICLE INFO

Article history:
Received 27 March 2021
Revised 26 June 2021
Accepted 28 June 2021
Available online 29 June 2021

Keywords:
PVD thin film
Nanoporous supercapacitor
Specific capacitance
porous CrN

ABSTRACT

Transition metal nitrides (TMN) have received widespread consideration as supercapacitor materials for a variety of energy storage applications. An important requirement to such electrode materials is a very high specific surface area, which is typically obtained through a percolating pore-network. Here, we use arc ion plating to prepare CrN-Ni composite coatings with 0, 30.4, 54.2, and 77.6 at.% Ni. Detailed X-ray diffraction and X-ray photoelectron spectroscopy showed that the coatings consist of CrN phases next to metallic Ni. Post-deposition treatments with HCl solutions lead to selective leaching, causing a porous nanostructure for the Ni-containing CrN coatings. From there, the coating with 54.2 at.% Ni in its as-deposited state provided the highest (electrode-geometric-area)-specific capacitance after the HCl treatment, giving 58.5 mF·cm^{-2} at 1.0 mA·cm^{-2} in a 0.5 M H_2SO_4 aqueous electrolyte. This value is about 80 times higher than for the as-deposited coatings or the Ni-free CrN. Consequently, our strategy to combine TMNs with metallic Ni and its subsequent treatment with HCl is highly effective in enlarging the specific surface area and adsorption sites. It allows to significantly enhance the energy storage performance of TMN thin film supercapacitors.

1. Introduction

Owing to the high charge–discharge efficiency, long service life and environmental compatibility, supercapacitors (SCs) have received widespread consideration to be used alone – or in combi-

---

* Corresponding authors.
E-mail addresses: tfzhang@gdut.edu.cn (T.F. Zhang), qmwang@gdut.edu.cn (Q. Wang).

https://doi.org/10.1016/j.matdes.2021.109949
0264-1275/© 2021 Published by Elsevier Ltd.

nation with other energy storage options – to offer improved power efficiency and enhanced cycle life. Therefore, SCs are available for many energy storage applications, such as regenerative braking, short-term energy storage, miniaturized energy storage devices, and emergency power supplies [1–4]. Typically, there are two storage mechanisms for SCs: 1) electrochemical double-layer capacitors (EDLC, electrochemical adsorption/desorption only occur on the surface of the electrodes, like carbons) and 2) pseudo-capacitor (electrosorption, reduction–oxidation reactions, and intercalation processes, like oxides). Thus, an ideal SC should have a high specific surface area for charge adsorption and/or chemical reaction [5,6]. As the most important constituent of SCs, various electrode materials have been extensively developed in recent years, both in their compositional and morphological design. The most common one is shaping high conductive carbon-based materials to specific morphologies (such as, nanotube, nanofiber, nanowire, nanoflower, and nanorods [7,8]), which are then covered with transition metal oxides (TMO, such as Co_3O_4, MnO_2, Nb_2O_5, TiO_2, TiO_3, HfO_2,and RuO_2) [9–19] to obtain their combinations as TMO@C or TMO/C. The other option is to dope the shaped carbon with N/O/S/P [20–26]. This is a mutually beneficial cooperation of EDLC and pseudocapacitor, getting a massively increased specific surface area for chemical reactions and charge absorptions, and greatly increasing energy density [27]. The comparison of their specific capacitance is depicted in the supplementary data, in Table S1. However, their fabrication is quite complicated and sometimes not eco-friendly, involving hydrofluoric acid etching and annealing.

Except for carbons and oxides, there are also lots of other SC electrodes, such as carbides (e.g., TiC [28]), sulfides (e.g., TiS [29]), nitrides (e.g., TiN [30]), and borocarbonitrides [31]. Among them, the physical vapor deposited (PVD) transition metal nitride (TMN) thin films are very promising [32]. The reported TMN electrodes, such as CrN [33–35], TiN [30,36,37], VN [38,39], Mo_2N [40–42], and TiNbN [43] have exhibited good performance in service life, as a result of their high conductivity, high structural and chemical stability, and have found also their position for supercapacitor applications. PVD techniques, especially magnetron sputtering and arc ion plating, are widely used in high-quality TMN coating fabrication [44,45]. PVD-produced transition metal nitride (TMN) film electrodes have many advantages over traditional powder-type electrode materials, including binder-free fabrication, good adhesion, uniformity, and easily controlled composition and thickness. This makes them promising candidates for flexible thin-film supercapacitors and on-chip micro-supercapacitors. The specific capacitance of TMN electrode materials is based on the high-speed electrostatic adsorption. Storing the charge on the electrodes and the interface of active materials at the electrolyte, requires a very large relative ion-accessible surface area. Therefore, the main work of the present study focuses on how to obtain a sufficiently porous structure and rough surface of PVD TMN thin films. Recently we showed that the (electrode-geometric-area)-specific capacitance C_a of magnetron sputtered ~ 1-μm-thin HfN can be improved from 0.7 to 5.6 $mF \cdot cm^{-2}$ by a post-deposition etching with Ar plus Kr ion beams, enlarging its specific surface area [46]. This is in the range of magnetron sputtered TiN, exhibiting a C_a value of ~ 3 $mF \cdot cm^{-2}$ for the ~ 1-μm-thin film, increasing to 8.8 $mF \cdot cm^{-2}$ for the 2.2-μm-thin film [36]. CrN (1.1 μm thin) provides already in its as-deposited state – by conventional magnetron sputtering – a much higher C_a value of 12.8 $mF \cdot cm^{-2}$ [34], which further can be improved to 17.7 $mF \cdot cm^{-2}$ [33] or even 35.4 $mF \cdot cm^{-2}$ [35] using glancing angle deposition. When preparing a porous CrN out of a magnetron co-sputtered CrN-Cu coating – by a subsequent selective chemical etching for 3–4 days with an 0.5 M HNO_3 – the specific capacitance can also be improved to 31.3 $mF \cdot cm^{-2}$ [47]. Here, we use a corresponding technique, but show that through the combination of CrN with Ni a faster formation of the porous structure can be obtained (3 h in 3 M HCl) allowing for a specific capacitance of even 58.5 $mF \cdot cm^{-2}$. All these C_a values refer to a current density of 1.0 $mA \cdot cm^{-2}$ or a scanning rate of 100 $mV \cdot s^{-1}$, further data of some literature values are given in the Table S1.

Previously reported works have been mainly focusing on the optimization of material selection, composition, and deposition parameters of the thin films, while in this study, a novel microstructure design strategy was applied to synthesize nanoporous thin film electrodes through PVD and subsequent selective chemical etching processes. This combined procedure for CrN-Ni thin films showed a remarkably enhanced capacitive performance as compared with other reported thin film systems. Generally, the combination of nitride coatings with Cu [48–52], Ni [53–55], Ta [56], or Ag [57,58], is warmly welcome for reducing the friction coefficient, enhancing the toughness, increasing plastic deformation and corrosion resistance. The ductile metallic phase is percolating throughout the typically brittle, but corrosion resistant TMN matrix [59]. Here, we used arc ion plating to prepare a CrN matrix – CrN combines high strength [60] with excellent corrosion [61] and oxidation resistance [62], and specific capacitance [34] – in which metallic Ni is uniformly distributed. After the deposition, the Ni is thoroughly etched away using an HCl solution, to prepare a sponge-like CrN coating. A schematic illustration of the fabrication process of the porous CrN thin films is shown in Fig. 1. We provide a detailed study on how the Ni content and the chemical etching parameters influence the microstructure, morphology, and electrochemical properties of these CrN-Ni thin films. The maximum (electrode-geometric-area)-specific capacitance value for the porous (after etching) CrN–Ni thin films exceeds those of the as-deposited CrN–Ni and CrN by a factor of ~ 80. The strategy outlined here, can be universally applied for modifying the surface and cross-sectional morphology of TMN films and enlarge their specific surface area and adsorption sites. This procedure shows great potential for optimizing the energy storage performance of TMN thin film supercapacitors.

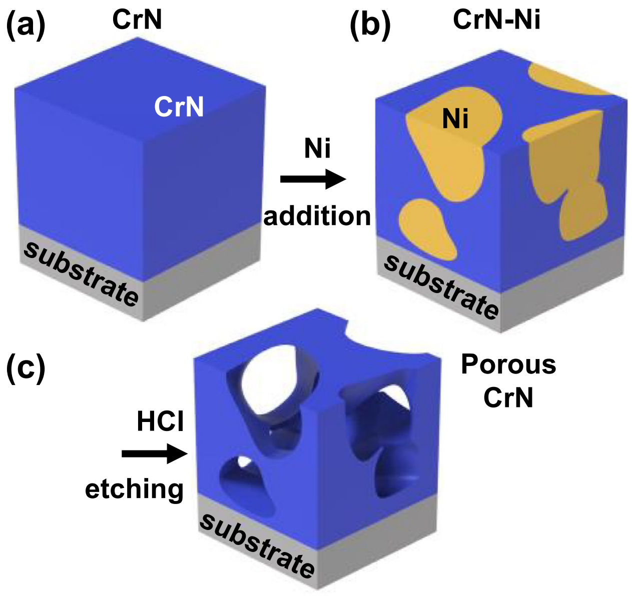

Fig. 1. Schematic illustration of the fabrication process for porous CrN thin films: (**a**) as-deposited CrN, (**b**) as-deposited CrN–Ni, and (**c**) porous CrN films.

2. Experimental

2.1. Samples preparation

CrN–Ni thin films with various Ni contents were deposited by arc ion plating (MD800, DG Huasheng, Inc.) using a Cr target (99.95% purity) and a $Ni_{80}Cr_{20}$ (20 at.% Cr) alloy target (99.95% purity). These two targets are placed horizontally at an angle of 100° to each other facing the substrate holder, which rotated with a speed of 1.5 rpm during the deposition, at a mean distance of 20 cm. The polished monocrystalline Si (1 0 0)-oriented substrates ($10 \times 10 \times 0.5$ mm^3) were ultrasonically cleaned in ethanol and deionized water successively and dried by nitrogen gas before being mounted to the substrate holder. The system was evacuated to a base pressure of at least 5×10^{-3} Pa. Prior to deposition, a 30-min etching process using Ar^+ and Kr^+ from a booster ion source (Pinnacle, Advanced Energy, Inc.) was conducted with a pressure of 2.0 Pa and a pulsed substrate bias potential of − 600 V to remove oxides and contaminants from the surface. Afterwards, a CrN adhesion layer (~0.3 μm thin) was deposited using 1.0 Pa N_2 atmosphere, 100 A target current, and − 100 V pulsed bias potential. The subsequent CrN–Ni layer (~0.7 μm thin) was deposited with the same N_2 atmosphere of 1.0 Pa, pulsed bias potential of − 100 V, and deposition temperature of 400 °C. The Ni content of these CrN–Ni top layers was varied by adjusting the current applied to the $Ni_{80}Cr_{20}$ and Cr targets, as listed in Table 1, using a pulsed DC power supply (DSP12A1, ZONGXINDA, Chengdu, Ict.) and adjusting the duty cycle to 15% and the frequency to 10 kHz.

We systematically varied the concentration of Ni in the CrN–Ni top layer (from 0 to 78 at.%), the exposure time in the HCl solution (from 1 to 18 h), and the intensity of the HCl solution (from 1 to 4 $mol \cdot l^{-1}$). During this etching process, the samples were removed from the HCl solution every hour, and washed with deionized water, dried with nitrogen, and tested for their specific capacitance.

2.2. Structural and chemical characterizations

The surface and cross-section morphologies of the as-deposited thin films and their best (classified through their area-specific capacitance) porous products (after the HCl solution treatment) were investigated by scanning electron microscopy (SEM, FEI Nova NanoSEM 430) at an accelerating voltage of 15 kV. The chemical composition of the samples was determined by using an integrated energy dispersive X-ray spectroscopy (Oxford instruments X-Max^N). The surface morphology of the thin films was also measured using atomic force microscopy (AFM, Bruker Dimension FastScan), with a dimension of 20×20 μm^2, in peak force tapping mode. The root-mean-square roughness (R_q) was calculated from three consecutive measurements for each sample. X-ray diffraction (XRD) in a Bragg–Brentano configuration, using a Bruker D8 Advance diffractometer (Cu Kα X-ray source, 40 kV, and 40 mA), was employed to investigate the crystal structure of the thin films. The chemical bonding states of the thin films were studied by X-ray photoelectron spectroscopy (XPS) with a Thermo Fisher Escalab 250Xi spectrometer using a monochromatic Al Kα source (15 kV and 15 mA). Initially, individual element survey scans were performed to detect the elements in all samples. Prior to these measurements, the surface of the coatings was Ar-ion etched (with an energy of 3 keV over an area of 3×3 mm^2) for 3.5 min to remove surface contaminants. The recorded spectra were calibrated by the C 1 s binding energy of 284.8 eV.

2.3. Electrochemical characterizations

An electrochemical workstation (AMETEK, 1470E) with a conventional three-electrode setup (working electrodes: the coatings presented here; reference electrode: Ag/AgCl [KCl saturated]; counter electrode: Pt plate), was used to evaluate the electrochemical properties of as-deposited and etched CrN-Ni thin films in a 0.5 M H_2SO_4 aqueous electrolyte. The specific capacitance was measured by cyclic voltammetry (CV) and galvanostatic charge–discharge (GCD), at a controlled potential window, scan rate, and current density. The conductivity and interfaces were investigated using electrochemical impedance spectroscopy (EIS), at an open-circuit voltage of 0.6 V, a disturbing voltage of 5 mV, and a frequency range of 0.01 – 100000 Hz. The cycling stability was tested by CV measurements at a constant scan rate of 100 $mV \cdot s^{-1}$ for 2000 cycles at room temperature.

The (electrode-geometric-area)-specific capacitance (C_a, $mF \cdot cm^{-2}$) of the thin film supercapacitors was calculated from galvanostatic charge–discharge by using [34]:

$$C_a = (I \times \Delta t)/S \times \Delta U \tag{1}$$

where I (mA) is the discharge current, Δt (s) is the discharge time, ΔU (V) is the potential window between the lowest and the highest potentials (U_a and U_b, respectively), and S (cm^2) is the geometric area of the working electrode.

Integrating the area of one CV cycle, the specific capacitance of the thin film supercapacitors can also be obtained, using the following equation [34]:

$$C_a = \int_{U_b}^{U_a} I(V)dV/2 \times \nu \times S \times (U_a - U_b) \tag{2}$$

where $\int_{U_b}^{U_a} I(V)dV$ is the integral current area and ν ($mV \cdot s^{-1}$) is the scan rate. This was used to calculate the retention rate of the capacitance during the 2000 cycle service life investigation.

3. Results and discussions

3.1. Structure and morphology

The chemical compositions of the as-deposited CrN–Ni thin films and those after a distinct HCl solution treatment (next paragraph) are given in Table 1. For easier reading, our thin films are named as CrN, CrN-Ni_{30}, CrN-Ni_{54}, and CrN-Ni_{78} according to their Ni-content of 0, 30.4, 54.2, and 77.6 at.% in the as-deposited state, respectively. This increase in Ni-content is obtained by incrementally increasing the arc ion plating current at the $Ni_{0.8}Cr_{0.2}$ target

Table 1
Target currents, etching time, and compositions of the CrN–Ni thin films in the as-deposited state and after the treatment in a 3.0 $mol \cdot l^{-1}$ HCl bath (indicated with an asterisk).

Sample	CrN	CrN*	CrN-Ni_{30}	CrN-Ni_{30}*	CrN-Ni_{54}	CrN-Ni_{54}*	CrN-Ni_{78}	CrN-Ni_{78}*
Cr target current (A)	90		90		80		0	
$Ni_{80}Cr_{20}$ target current (A)	0		50		80		90	
3.0 M HCl etching time (h)		18		11		3		4
N (at.%)	48.9	49.9	36.5	50.0	15.1	49.4	8.3	23.7
Cr (at.%)	51.1	50.1	33.1	41.8	20.7	43.5	14.1	22.3
Ni (at.%)	0	0	30.4	8.2	54.2	7.1	77.6	54.0

from 0 to 90 A and simultaneously decreasing the current at the Cr target from 90 to 0 A, see Table 1. Therefore, their Cr and N contents decreased continuously from around 50 to 10 at.%.

Detailed studies on the effect of the HCl solution concentration over the potential range from −0.2 and 0.8 V showed best results in current density for the CrN-Ni$_{54}$ thin film (as measured by the cyclic voltammetry (CV) at a scan rate of 100 mV·s^{-1} and galvanostatic charge–discharge (GCD) at a current density of 1.0 mA·cm^{-2}), when using a 3.0 mol·l^{-1} concentration (the curves for the individual HCl concentrations are provided in the supplementary data Fig. S1). The area-specific capacitance C_a of the Ni-containing samples CrN-Ni$_{30}$, CrN-Ni$_{54}$, and CrN-Ni$_{78}$ peaked with 11 h, 3 h, and 4 h of dissolution time within the 3.0 M HCl bath, respectively, see Fig. 2a (and supplementary data Fig. S2). The samples providing the C_a peak-values are indicated with an asterisk: CrN-Ni$_{30}$* (11 h treatment time), CrN-Ni$_{54}$* (3 h treatment time), and CrN-Ni$_{78}$* (4 h treatment time). As expected, there is no change for the Ni-free CrN thin film, but the sample CrN* refers to the maximum treatment time of 18 h in the 3.0 M HCl solution. Fig. 2b shows the C_a peak-values for our samples with respect to the C_a values in their as-deposited state, obtained at a current density of 1.0 mA·cm^{-2}. This comparison clearly shows that the highest C_a value with ~ 58.5 mF·cm^{-2} is obtained with the CrN-Ni$_{54}$ coating (54.2 at.% Ni), followed by ~ 18.0 mF·cm^{-2} for the CrN-Ni$_{78}$ coating (77.6 at.% Ni). When compared to their as-deposited condition, the CrN-Ni$_{30}$, CrN-Ni$_{54}$, and CrN-Ni$_{78}$ coatings experienced an increase in their C_a values by a factor of ~ 16, 80, and 11, respectively, clearly highlighting the massive improvement in C_a due to the HCl treatment. This is because, by the HCl treatment a porous structure is formed, which will be presented later. The Ni content of the samples massively decreased due to the HCl solution treatment, from 30.4 to 8.2 at.% for CrN-Ni$_{30}$, from 54.2 to 7.1 at.% for CrN-Ni$_{54}$, and from 77.6 to 54.0 at.% for CrN-Ni$_{78}$, see Table 1. As expected, the chemical composition of the Ni-free CrN sample shows no obvious difference before and after 18 h of HCl etching, indicating the excellent chemical stability of CrN. Due to the etching procedure – as most of the Ni is etched away especially for the CrN-Ni$_{30}$ and CrN-Ni$_{54}$ coatings – also their overall Cr content increased to 41.8 and 43.5 at.%, respectively, Table 1. The HCl solution nicely changed its color into green, due to Ni dissolution (Fig. S3, supplementary data). Due to the very high Ni content of the CrN-Ni$_{78}$ coating – basically a Ni matrix with CrN precipitates is formed – chemical etching with the 3.0 M HCl would require significantly longer times for a more pronounced dissolution. The removal of Ni from the CrN-Ni$_{30}$ and CrN-Ni$_{54}$ coatings is promoted by their high fraction of phase-boundaries between Ni and CrN supporting access of the HCl solution.

XRD investigations of the as-deposited coatings show the face centered cubic (fcc) CrN phase, see their (1 1 1) and (2 0 0) diffraction peaks at 37.5 and 43.7° in Fig. 3a. The small peak at the left-hand shoulder of the (2 0 0) fcc CrN peak for the CrN-Ni$_{54}$ coating might indicate the presence of a small fraction of the hexagonal Cr$_2$N phase. For the other coatings, this is probably hidden behind their relatively broader XRD peaks. With increasing Ni-content, the XRD peaks at 44.5 and 51.8° (indicative for the (1 1 1) and (2 0 0) lattice plane distances of fcc-Ni) increase in intensity. No nickel nitride phase could be detected, in agreement to the known weak nitride forming tendency of Ni [63]. After the HCl solution treatment, almost no crystalline Ni phase can be detected anymore for CrN-Ni$_{30}$* and CrN-Ni$_{54}$*, see Fig. 3b. Contrary, the CrN-Ni$_{78}$* coating still shows a pronounced crystalline Ni phase content in agreement with the chemical investigations, see Table 1. The profile of the XRD peaks from the CrN phase did not change due to the HCl solution treatment (please compare Fig. 3a and b), especially when considering the changed contribution from the Ni phase. This furthermore indicates the excellent chemical stability and corrosion resistance of CrN.

SEM top view investigations of the coatings clearly show the formation of a porous structure due to the HCl solution treatment, when Ni was present in the as-deposited state. The Ni-free CrN thin film exhibits a dense and smooth surface before and after etching, see Fig. 4a and b, respectively, again underlining the excellent corrosion resistance of CrN [64]. The 30.4 at.% Ni containing sample (CrN-Ni$_{30}$) shows some small particles at the surface (Fig. 4c), which were removed by the etching treatment (CrN-Ni$_{30}$*, Fig. 4d). The sensitivity to the HCl solution treatment suggests these particles to be metallic Ni. Independent on the HCl solution treatment-time, the surface of this sample always was rather smooth, indicating that the Ni content of this sample (CrN-Ni$_{30}$) is too low to allow its complete percolation throughout the matrix. In other words, the metallic Ni phase is not interconnected but rather present as pockets encapsulated by the corrosion-resistant ceramic CrN.

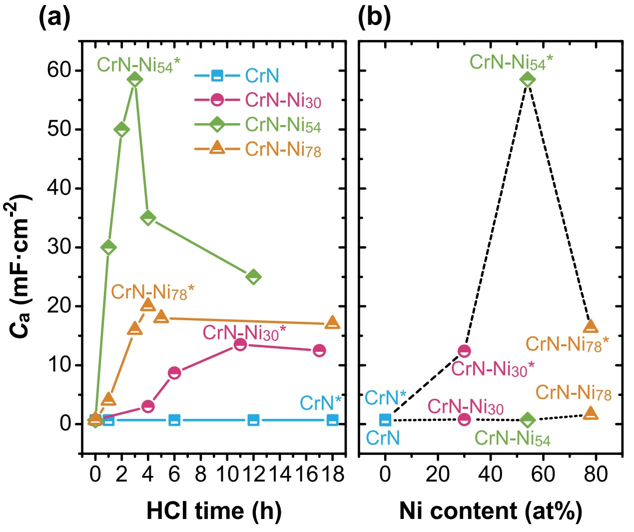

Fig. 2. (a) Comparison of specific capacitance of the coatings CrN, CrN-Ni$_{30}$, CrN-Ni$_{54}$, and CrN-Ni$_{78}$ after different immersion times in HCl solution (current density: 1.0 mA·cm^{-2}). (b) Comparison of the peak-values in specific capacitance of these samples to their as-deposited state (current density: 1.0 mA·cm^{-2}).

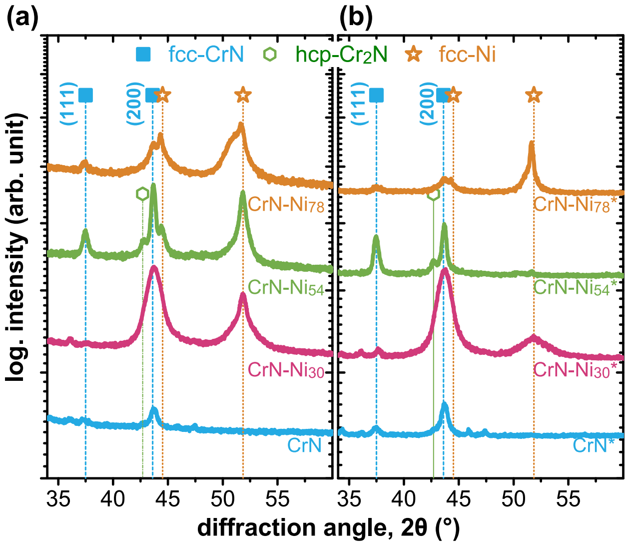

Fig. 3. XRD patterns of (a) as-deposited coatings and (b) coatings after the HCl treatment for various times to obtain their highest specific capacitance (Fig. 2).

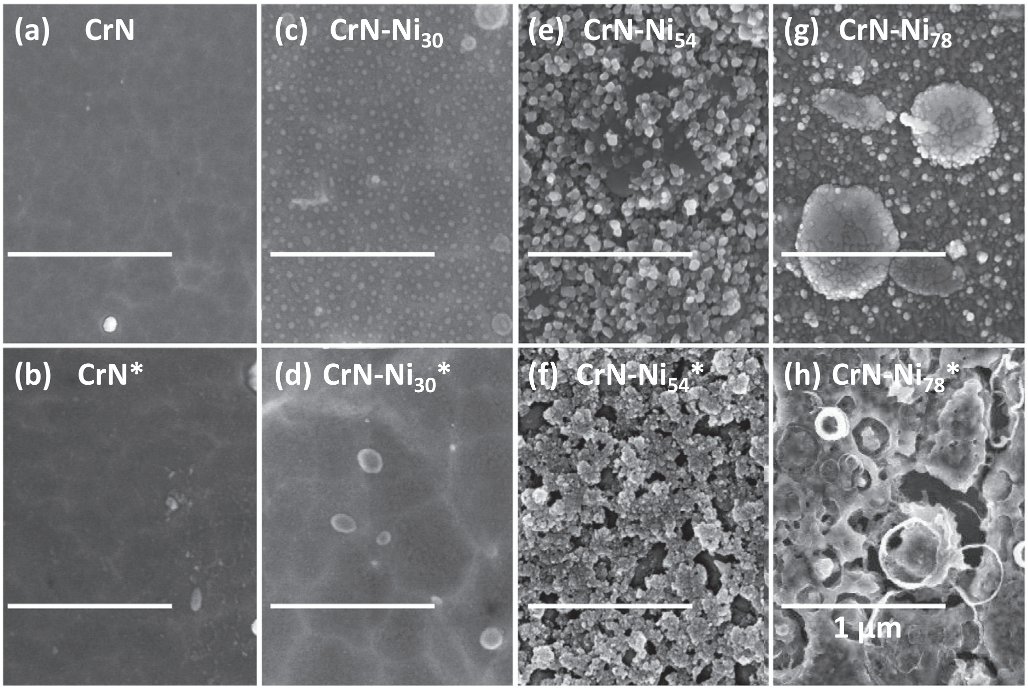

Fig. 4. Top-view SEM images of CrN **(a and b)**, CrN-Ni_{30} **(c and d)**, CrN-Ni_{54} **(e and f)**, and CrN-Ni_{78} **(g and h)** coatings in their as-deposited state and after the HCl treatment to obtain their highest specific capacitance (Fig. 2), respectively. The white horizontal line has the same length in all SEM images and represents the scale bar of 1 µm.

The CrN-Ni_{54} coating (54.2 at.% Ni) shows much larger particles at the surface already in its as-deposited state, Fig. 4e. After the 3 h treatment in the HCl bath, the SEM top-view investigations already indicate for a sponge-like morphology with a high porosity (CrN-Ni_{54}*, Fig. 4f). Consequently, here the Ni content was sufficiently high to allow for the formation of an interconnected Ni-network in the as-deposited state. Our data furthermore show that the HCl solution treatment-time needs to be controlled, to allow that most of the Ni-phase is dissolved, leading to a maximization of the porosity. However, if the treatment time is too long, the remaining CrN-skeleton may be separated from the CrN adhesion layer and influence the electrodes' service life.

The impressions from the top-view SEM investigations are in-line with detailed AFM analysis (supplementary data Fig. S4, scanning over a surface area of 20 × 20 μm^2) yielding root mean square roughness (R_q) values of 7.8 and 152.0 nm for the coatings CrN and CrN-Ni_{54}, respectively. By the HCl solution treatment for 3 h, the R_q value of the CrN-Ni_{54} coating increased further to 185.0 nm. The SEM top-view investigations already indicated the increased surface roughness by this HCl solution treatment (compare Fig. 4e and f).

Further increasing the Ni content to 77.6 at.% leads to a coating (CrN-Ni_{78}) that shows already in the as-deposited state (Fig. 4g) a less promising surface quality than the CrN-Ni_{54} coating. The surface is characterized by fewer homogenously distributed particles, but some very large ones as well. After a 4 h treatment in the HCl bath, ring-shaped holes formed at the surface, suggesting that especially at the CrN–Ni interfaces the dissolution kinetic is faster. In general, these SEM investigations indicate that for this sample the Ni content is too high. Thus, out of the three Ni-containing CrN samples, the CrN-Ni_{54} coating showed the most promising formation of a porous material after the HCl solution treatment, based on these SEM top-view investigations.

Whether the formed pores also expand throughout the coating thickness was studied by SEM fracture cross-sections, Fig. 5. The Ni-free CrN thin film shows the most compact cross-sectional morphology in the as-deposited state (Fig. 5a), which is only a bit influenced by the HCl treatment for 18 h (Fig. 5b). In agreement with the plan-view SEM investigations (Fig. 4), also the cross-sectional morphology of the CrN-Ni_{30} coating is only slightly influenced by the HCl solution treatment. Considering the noticeable change in Ni content (from 30.4 down to 8.2 at.%) this is somehow surprising and suggests the formation of rather small pores. Contrary, the CrN-Ni_{54} coating shows a significant change in cross-sectional morphology across the entire thickness of the Ni-containing part, due to the HCl solution treatment. Already in its as-deposited state, this coating is characterized by a rather rough cross-sectional morphology due to the competitive growth of the Ni and CrN phases. These SEM studies nicely show that the generated pores (due to the dissolution of most of the Ni-phase, please remember that here the Ni-content decreased from 54.2 to 7.1 at.%) percolate throughout the entire outer CrN–Ni layer (Fig. 5f). The highest Ni containing coating, CrN-Ni_{78}, reveals a smoother appearance especially of the surface-near region in the as-deposited state (Fig. 5g), with even some pores present underneath this area. However, after the HCl solution treatment, no percolating pore-network formed (Fig. 5h). The studies furthermore show that all samples have nearly the same entire coating thickness of ~ 1.0 µm.

Based on these SEM top-view (Fig. 4) and SEM fracture cross-section (Fig. 5) studies, we can conclude that the most effective form of a fully percolating pore-network, due to the HCl solution treatment, is obtained for the 54.2 at.% Ni containing coating, CrN-Ni_{54}. This coating exhibits a high porosity after the HCl treatment (considering that the coating thickness remained the same, but its Ni content decreased from 54.2 to 7.1 at.%), with well-distributed pore-sizes (Fig. 6), where ~ 30-nm-sized ones build the highest fraction. According to Huang et al. [65], the most ideal pore size for providing aqueous electrolyte pools and fast ionic transport channels for supercapacitor electrodes is in the range 2–50 nm. Smaller pores (<2 nm) – smaller than the size of solvated electrolyte ions – do not contribute to energy storage, and larger pores (>50 nm) do not provide a sufficient specific surface. Although the CrN-Ni_{78}* is also very porous (Fig. 4h), the pore size is not nicely distributed. CrN-Ni_{54}* offers the highest area-

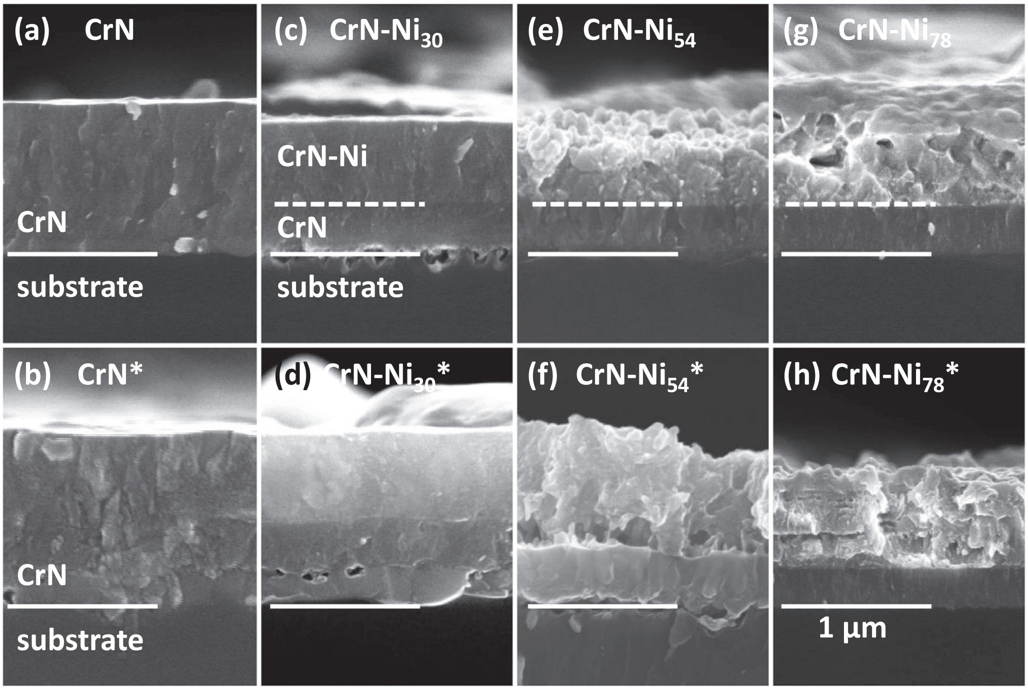

Fig. 5. Fracture cross-sectional SEM images of CrN (**a and b**), CrN-Ni_{30} (**c and d**), CrN-Ni_{54} (**e and f**), and CrN-Ni_{78} (**g and h**) coatings in their as-deposited state and after the 3.0 M HCl treatment to obtain their highest specific capacitance (Fig. 2), respectively. The solid and dashed white horizontal lines have the same length in all SEM images and represent the scale bar of 1 μm. The dashed line indicates the interface between CrN adhesion layer and CrN-Ni coating, the solid line indicates the interface between Si substrate and CrN adhesion layer.

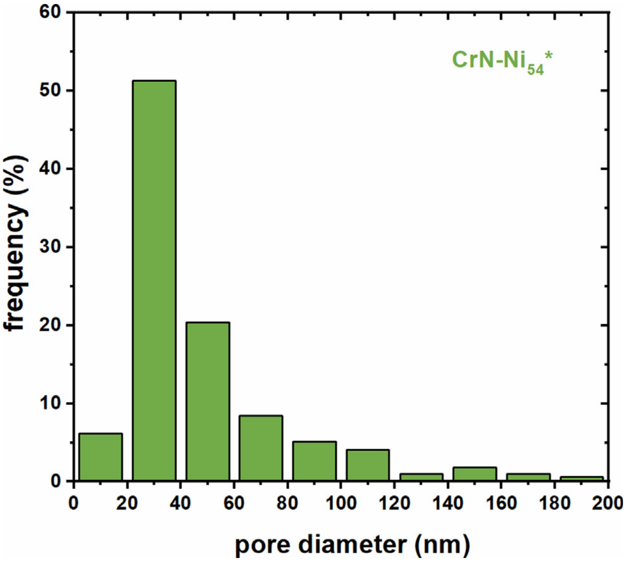

Fig. 6. Pore size distribution (as obtained by digital image processing of Fig. 4f) of the CrN-Ni_{54} after the 3.0 M HCl treatment (CrN-Ni_{54}*) to obtain its highest specific capacitance (Fig. 2).

specific capacitance C_a among all coatings and HCl-treated coatings studied, which is also depicted in Fig. 2.

This most promising sample, CrN-Ni_{54}, was studied in detail by XPS to characterize any changes in their chemical bonding states from the as-deposited state to the HCl-treated state. Before these measurements, their surface was Ar-ion etched to a depth of ~ 50 nm to avoid interference by unwanted surface contaminations. The XPS spectra of the CrN-Ni_{54} coating prior-to and after the HCl treatment are almost identical; therefore, we only briefly concentrate on the N 1 s, Cr 2p, and Ni $2p_{3/2}$ XPS core-level spectra. The N 1 s XPS core-level spectra of CrN-Ni_{54} (Fig. 7a) and CrN-Ni_{54}* (Fig. 7b) are very similar even with their contributions from CrN (binding energy between 396.5 and 397.8 eV [66]) and Cr_2N (binding energies between 397.5 and 398.0 eV). The major contribution comes from CrN, in agreement with XRD studies, which indicated only a tiny fraction of the Cr_2N phase. The Cr $2p_{3/2}$ XPS core-level spectra also suggest the presence of Cr_2O_3 (at 576.1 eV [67]), but also here, the features at 574.8 eV (indicative for CrN [67]) and 576.1 eV (indicative for Cr_2N) are almost identical prior-to and after the HCl treatment, Fig. 7c and d, respectively. A small contribution of Ni–O bonds next to the major metallic Ni (at about 852.8 eV) can also be concluded from the Ni $2p_{3/2}$ XPS core-level spectra of this sample prior-to and after the HCl treatment, Fig. 7e and f, respectively. In excellent agreement with XRD, the XPS studies do not show any Ni–N bonds in these films.

3.2. Electrochemical properties

To demonstrate the merits of the porous structure, we compared the electrochemical performance of our samples (CrN, CrN-Ni_{30}, CrN-Ni_{54}, and CrN-Ni_{78}) in their as-deposited state with that after the HCl treatment providing their C_a peak-values (CrN*, CrN-Ni_{30}*, CrN-Ni_{54}*, and CrN-Ni_{78}*) using a three-electrode system. The CV curves at a scan rate of 100 $mV\cdot s^{-1}$ show that the as-deposited samples (Fig. 8a) and the HCl treated samples (Fig. 8b) demonstrate appropriate symmetry, which allows for a good electric double-layer energy storage mechanism. The much more extensive range in current density for the HCl treated samples, the y-axis of Fig. 8b, than that of the as-deposited ones, Fig. 8a, is due to their massively higher C_a values. Similarly, the GCD curves, measured with a current density of 1.0 mA·cm-2, are nearly symmetric. The times for obtaining the discharge-peak also massively increase due to the HCl solution treatment. Please compare Fig. 8c and d, which again demonstrates the significant improvement in specific capacitance.

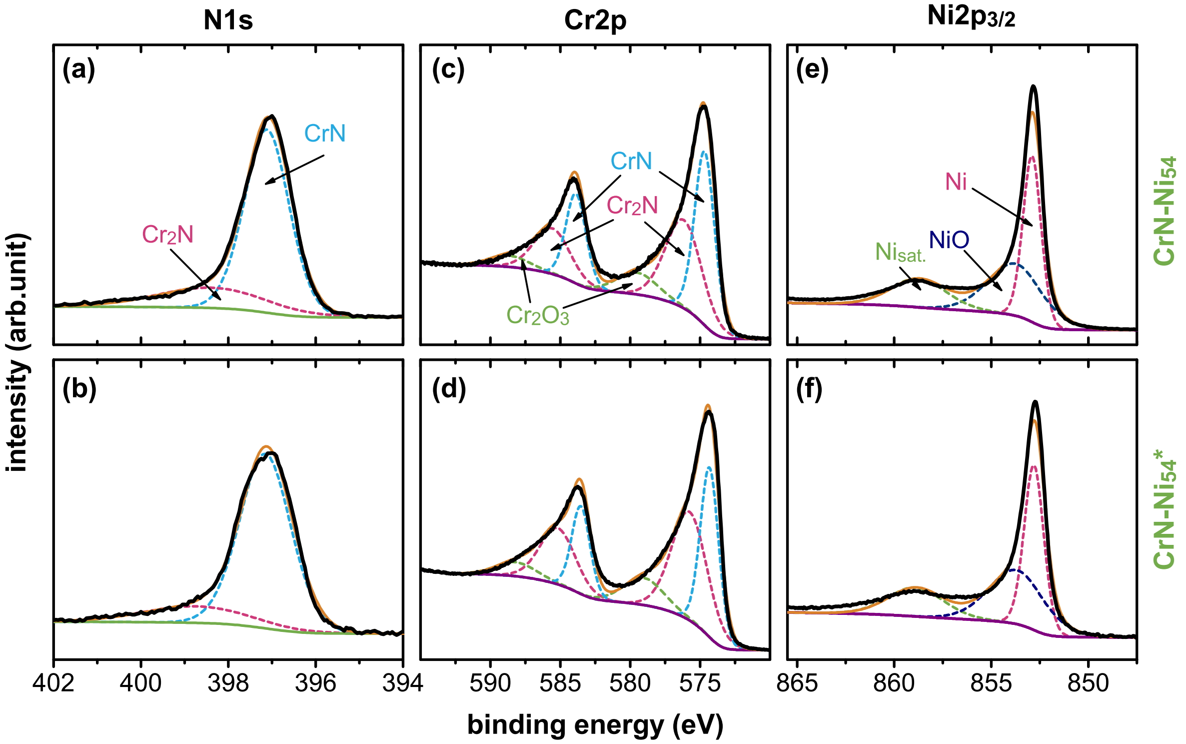

Fig. 7. XPS core-level spectra of **(a and b)** N 1 s, **(c and d)** Cr 2p, and **(e and f)** Ni $2p_{3/2}$ energy regions for the CrN-Ni_{54} coating in its as-deposited state (CrN-Ni_{54}) and after the 3.0 M HCl treatment (CrN-Ni_{54}*) to obtain its highest specific capacitance (Fig. 2), respectively.

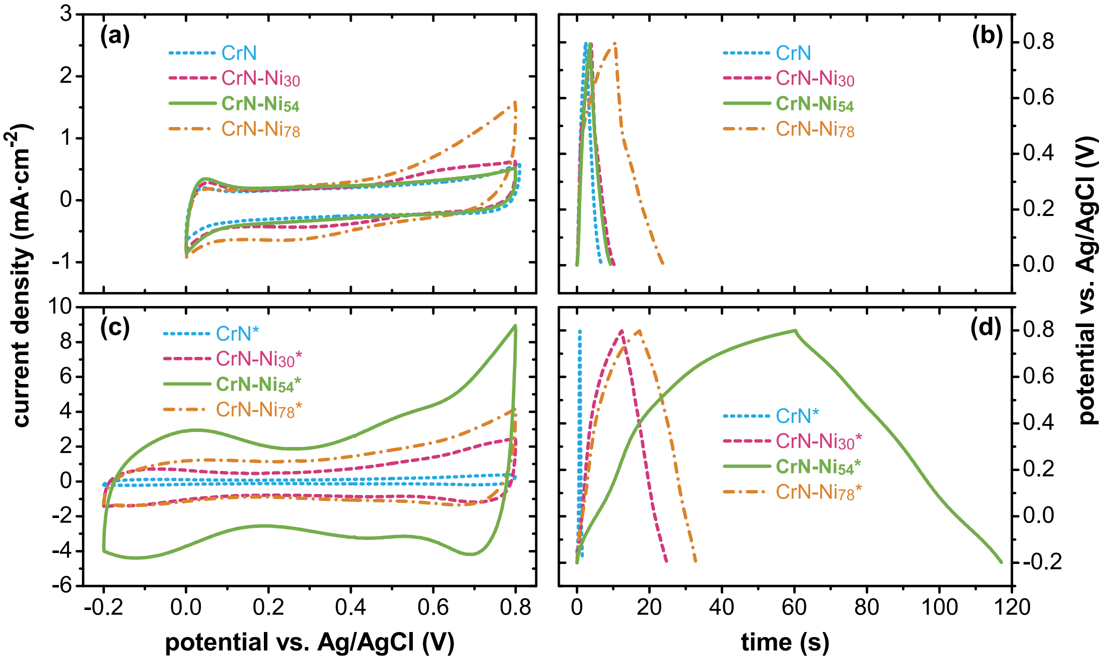

Fig. 8. **(a)** CV curves (scan rate: 100 mV·s^{-1}) and **(b)** GCD curves (current density: 1.0 mA·cm^{-2}) of CrN, CrN-Ni_{30}, CrN-Ni_{54}, and CrN-Ni_{78} in their as-deposited state. **(c)** CV curves (scan rate: 100 mV·s^{-1}) and **(d)** GCD curves (current density: 1.0 mA·cm^{-2}) of these coatings after 3.0 M HCl treatment to obtain their highest specific capacitance (CrN*, CrN-Ni_{30}*, CrN-Ni_{54}*, and CrN-Ni_{78}*).

Electrochemical impedance spectroscopy (EIS) was conducted to study the charge transfer and ion diffusion properties of the electrode materials. Fig. 9a and b show the Nyquist plots obtained by these EIS measurements of our samples in their as-deposited state and after the HCl solution treatment leading to their C_a peak-values, respectively. The insets show a detailed view of the high-frequency region, and the equivalent circuit diagram for these EIS measurements is given in Fig. 9c. Just for a brief recall: in such Nyquist plots, Z' and Z" represent the real and imaginary part of impedance, respectively. At the left side of these diagrams (close to 0 of Z' and Z", the high-frequency side) a semicircle followed by a straight line indicates capacitive behavior. Their small impe-

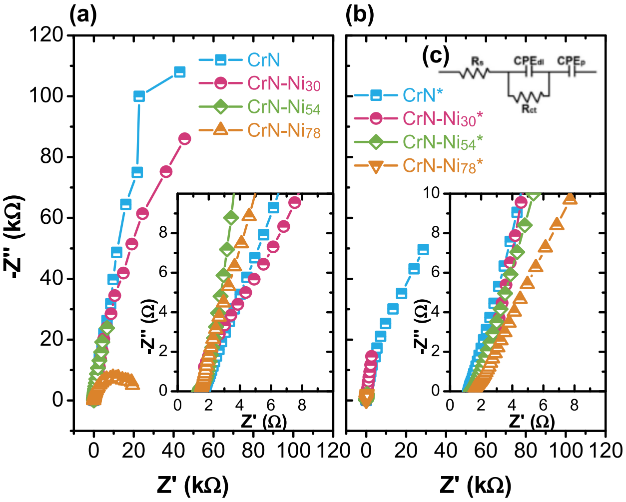

Fig. 9. Nyquist plots of CrN, CrN-Ni$_{30}$, CrN-Ni$_{54}$, and CrN-Ni$_{78}$ coatings in their as-deposited state **(a)** and after the 3.0 M HCl treatment to obtain their peak in their specific capacitance **(b)**. **(c)** Equivalent circuit diagram.

dance in the high-frequency region indicates meager charge transfer resistance (R_{ct}), a testament to their intrinsically outstanding electrical conductivity and electrochemical activity [68]. The highest frequency point (the first intersection with the x-axis) refers to the electrolyte resistance (R_s) because, at such high frequencies there is no resistance in capacitance. Therefore, they have similar R_s values, which are 1.2–1.5 Ω due to the resistance of the 0.5 M H_2SO_4 electrolyte [69]. The higher the imaginary part of impedance (hence the steeper the Nyquist curve), the easier the electrolyte can access the surface, and the materials exhibit ideal capacitive behavior [70], which is the case for all of our samples (as-deposited, Fig. 9a, or HCl treated, Fig. 9b) except for the highest Ni-containing coating in its as-deposited state (CrN-Ni$_{78}$). The HCl-treated samples show a smaller impedance range than the as-deposited ones, suggesting excellent capacitance behavior.

To further investigate the CrN-Ni$_{54}$ thin film electrode's suitability after the 3 h treatment in a 3.0 M HCl solution (CrN-Ni$_{54}$*) for potential applications, its capacitive behavior is studied by CV curves at different scan rates from 10 to 1000 mV·s^{-1}, see Fig. 10a. Notably, these CV curves show a gradual increase in current density, with quasi-rectangular shapes even up to 1000 mV·s^{-1}, indicating excellent capacitive behavior and high-rate capability. Fig. 10b depicts the CrN-Ni$_{54}$* electrode's GCD curves at current densities from 0.5 to 10 mA·cm^{-2}. The nearly symmetric potential–time curves for all current densities imply a high charge–discharge Coulombic efficiency (≥97%) and low polarization of this electrode material (supplementary data Fig. S5). With an increase of the current density from 0.5 to 10.0 mA·cm^{-2}, the area-specific capacitance C_a decreases from 62.5 to 42.2 mF·cm^{-2}. This relatively small reduction in C_a by 67.5% during this increase in current density, suggests good reversibility of the electrochemical reaction at the surface of the CrN-Ni$_{54}$* thin film. Corresponding Coulombic efficiency investigations of CrN-Ni$_{30}$* and CrN-Ni$_{78}$* are provided in the supplementary data, Fig. S5. They also depict roughly 100% charge–discharge Coulombic efficiency. The related studies of GCD and CV with different current densities and scan rates for CrN-Ni$_{30}$* and CrN-Ni$_{78}$* are provided in the supplementary data, Fig. S6. Compared with another porous CrN thin film, which was obtained by etching away the ~ 19 at% Cu from the CrN–Cu [47], the C_a value of the CrN-Ni$_{54}$* thin film (with 58.5 mF·cm^{-2} at 1.0 mA·cm^{-2}) is higher than the reported one of 33.1 mF·cm^{-2} (at 1.0 mA·cm^{-2}) for a porous CrN.

The cycling stability of the CrN-Ni$_{54}$* electrode was proven by 2000 successive CV measurement cycles using a scan rate of 100 mV·s^{-1}. The CV curves of the 1st and 1000th cycle have a similar shape but cover a slightly different area, being unchanged for the subsequent 1000 cycles, Fig. 10c. The capacitance retention, Fig. 10d, clearly shows that the CrN-Ni$_{54}$* electrode undergoes a more rapid decay down to 91.7% for the first 300 cycles, and after around 600 cycles, a steady-state behavior is obtained. Essentially, there is no change between the 600th and 2000th cycles, during

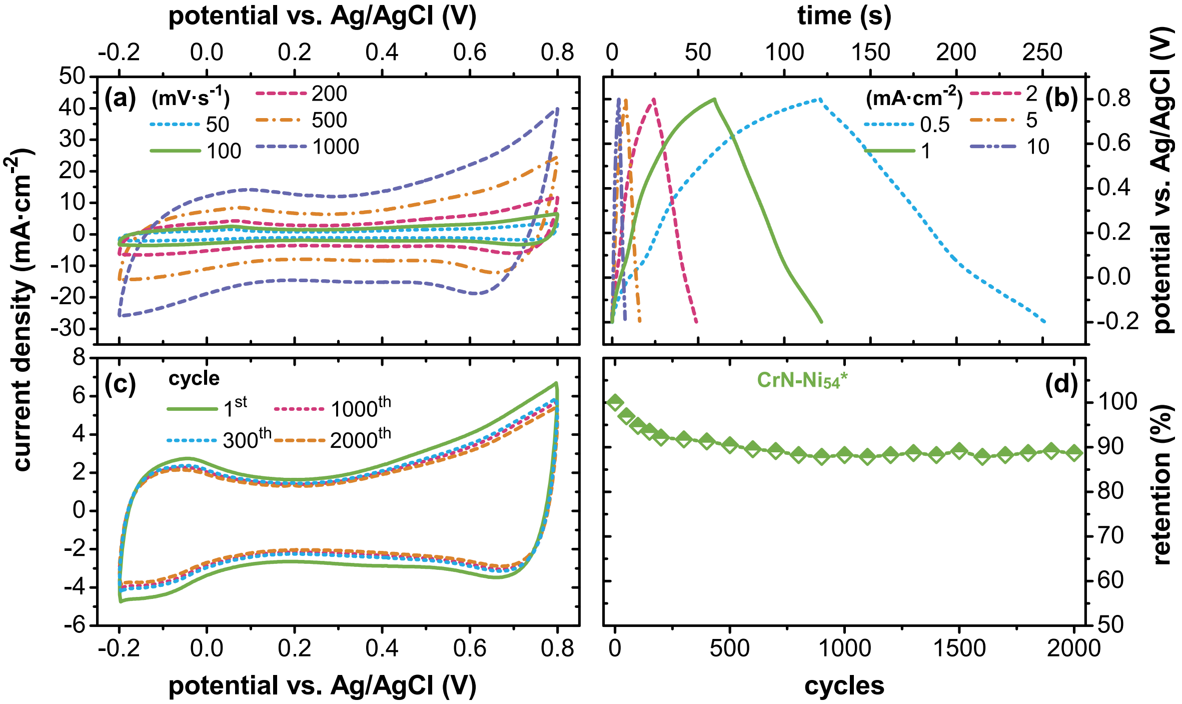

Fig. 10. **(a)** CV curves at different scan rates (in mV·s^{-1}), **(b)** GCD curves at different current densities (at mA·cm^{-2}), **(c)** CV curves of the 1st, 300th, 1000th and 2000th cycle and **(d)** cycling performance at a scan rate of 100 mV·s^{-1}, for the CrN-Ni$_{54}$ coating after the 3 h treatment time in a 3.0 M HCl bath (after which this coating reached its peak area specific capacitance, Fig. 2, due to the formation of a fine porous morphology, Figs. 4 and 5).

which still 88.5 ± 0.5% of the initial capacitance remains. The initial decrease in capacitance comes from the irreversible consumption of the electrode (basically remaining Ni) in the electrolyte. This leaves room to further optimize the pre-treatment procedure. However, the cycling performance is better than that of nitride-based electrodes prepared from nitridation of metal oxides, such as VN@CF (which exhibit 82% capacitance retention after 1000 cycles) [71]. Still, it seems to be slightly less stable than that of other nitride-based electrodes prepared by PVD, such as CrN (92.1% retention after 20,000 cycles) [34], TiVN (99% retention after 10,000 cycles) [72], and CrCuN (94% capacitance retention over 20,000 cycles) [47]. However, our data suggest that after the "running-in" period (for the first 600 cycles), a steady state behavior is obtained during which the area-specific capacitance of the CrN-Ni_{54}* film electrode is unchanged at 88.5 ± 0.5% ($C_a \cong 50.0$ mF·cm^{-2}) of its initial value (58.5 mF·cm^{-2}).

4. Summary and conclusions

We used arc ion plating and a combination of a Cr and $Ni_{80}Cr_{20}$ target to prepare ~ 0.7 μm thin CrN–Ni films with 0, 30.4, 54.2, and 77.6 at.% Ni on top of a ~ 0.3 μm thin CrN adhesion layer. XPS and XRD analyses indicate that the as-deposited CrN–Ni coatings are composed of CrN and metallic Ni phases, without any sign for a Ni–N phase. Post-deposition chemical treatments with HCl solutions of different concentrations and exposure times led to the formation of an interconnected fully percolating pore-network in the Ni-containing parts, as proven by detailed top-view and fracture cross-sectional SEM investigations. Here, specifically, the CrN–Ni film that contained 54.2 at.% Ni in the as-deposited state provided the highest porosity with an average pore size of 30 nm after a 3-h-treatment with 3.0 mol·l^{-1} HCl solution (during which the Ni content decreased to 7.1 at.%).

The electrochemical performance of the HCl-treated CrN–Ni films – benefiting from the porous structure and high specific surface area – was much better than that of the as-deposited CrN and CrN–Ni films. The nanoporous coating that we obtained by the HCl treatment of the 54.2 at.% Ni containing CrN–Ni film, achieved the highest area-specific capacitance of 58.5 mF·cm^{-2} at 1.0 mA·cm^{-2} upon all CrN–Ni films investigated. This value is by a factor of ~ 80 higher than that of the as-deposited CrN and CrN–Ni thin films. Furthermore, this coating also provides an excellent capacitance retention rate. After an initial decay to 88.5 ± 0.5% during the first 600 cycles, a steady-state behavior (with $C_a \cong 50.0$ mF·cm^{-2}) is obtained where the retention rate did not change up to 2000 cycles (highest number of charge–discharge cycles tested here). Based on our results, we can conclude that the combination of transition metal nitrides with Ni and the post-deposition treatment with HCl is very effective in preparing porous transition metal nitrides with a high specific surface area. This allows for the efficient preparation of solid-state thin film supercapacitors.

5. Data Availability

The raw/processed data required to reproduce these findings cannot be shared at this time as the data also are part of an ongoing study.

Declaration of Competing Interest

The authors declare that they have no known competing financial interests or personal relationships that could have appeared to influence the work reported in this paper.

Acknowledgements

This work was supported by the projects of the National Natural Science Foundation of China (Grant No. 51875109), and Natural Science Foundation of Guangdong Province of China (Grant No. 2020A1515010968), and the National Key Research and Development Project of China (Grant No. 2017YFE0125400). ZG thanks the support of the State Scholarship Fund of China (No. 201908440933) during her PhD at TU Wien.

Appendix A. Supplementary material

Supplementary data to this article can be found online at https://doi.org/10.1016/j.matdes.2021.109949.

References

[1] S. Bouhtiyya, R. Lucio Porto, B. Laïk, P. Boulet, F. Capon, J.P. Pereira-Ramos, T. Brousse, J.F. Pierson, Application of sputtered ruthenium nitride thin films as electrode material for energy-storage devices, Scr. Mater. 68 (2013) 659–662, https://doi.org/10.1016/j.scriptamat.2013.01.030.

[2] N.A. Kyeremateng, T. Brousse, D. Pech, Microsupercapacitors as miniaturized energy-storage components for on-chip electronics, Nat. Nanotechnol. 12 (2017) 7–15, https://doi.org/10.1038/nnano.2016.196.

[3] V.S. Bagotsky, A.M. Skundin, Y.M. Volfkovich, Electrochemical Power Sources: Batteries, Fuel Cells, and Supercapacitors (2015).

[4] M. Acerce, D. Voiry, M. Chhowalla, Metallic 1T phase MoS_2 nanosheets as supercapacitor electrode materials, Nat. Nanotechnol. 10 (2015) 313, https://doi.org/10.1038/nnano.2015.40.

[5] Y. Shao, M.F. El-Kady, J. Sun, Y. Li, Q. Zhang, M. Zhu, H. Wang, B. Dunn, R.B. Kaner, Design and mechanisms of asymmetric supercapacitors, Chem. Rev. 118 (2018) 9233–9280, https://doi.org/10.1021/acs.chemrev.8b00252.

[6] B.E. Conway, Electrochemical Supercapacitors: Scientific Fundamentals and Technological Applications, Springer, Boston (1999), https://doi.org/10.1007/978-1-4757-3058-6.

[7] M.S. Balogun, Y. Huang, W. Qiu, H. Yang, H. Ji, Y. Tong, Updates on the development of nanostructured transition metal nitrides for electrochemical energy storage and water splitting, Mater. Today 20 (2017) 425–451, https://doi.org/10.1016/j.mattod.2017.03.019.

[8] T.F. Zhang, Q.X. Xia, Z.X. Wan, J.M. Yun, Q.M. Wang, K.H. Kim, Highly porous carbon nanofoams synthesized from gas-phase plasma for symmetric supercapacitors, Chem. Eng. J. 360 (2019) 1310–1319, https://doi.org/10.1016/j.cej.2018.10.220.

[9] Q. Zhang, X. Wang, Z. Pan, J. Sun, J. Zhao, J. Zhang, C. Zhang, L. Tang, J. Luo, B. Song, Z. Zhang, W. Lu, Q. Li, Y. Zhang, Y. Yao, Wrapping Aligned Carbon Nanotube Composite Sheets around Vanadium Nitride Nanowire Arrays for Asymmetric Coaxial Fiber-Shaped Supercapacitors with Ultrahigh Energy Density, Nano Lett. 17 (2017) 2719–2726, https://doi.org/10.1021/acs.nanolett.7b00854.

[10] W. Raza, F.Z. Ali, N. Raza, Y.W. Luo, K.H. Kim, J.H. Yang, S. Kumar, A. Mehmood, E.E. Kwon, Recent advancements in supercapacitor technology, Nano Energy 52 (2018) 441–473, https://doi.org/10.1016/j.nanoen.2018.08.013.

[11] F. Beguin, V. Presser, A. Balducci, E. Frackowiak, Carbons and electrolytes for advanced supercapacitors, Adv. Mater. 26 (2014) 2219-51, 2283. https://doi.org/10.1002/adma.201304137

[12] K. Karuppasamy, D. Vikraman, J.H. Jeon, S. Ramesh, H.M. Yadav, V.R. Jothi, R. Bose, H.S. Kim, A. Alfantazi, H.S. Kim, Highly porous, hierarchical microglobules of Co3O4 embedded N-doped carbon matrix for high performance asymmetric supercapacitors, Appl. Surf. Sci. 529 (2020), https://doi.org/10.1016/j.apsusc.2020.147147.

[13] T. Xia, Q.H. Wang, W.L. Wu, C.H. Ao, Z. Zheng, C.H. Lu, Z.M. Chen, W. Zhang, Fabrication and characterization of MnO2-Coated carbon fabrics from silk for shape-editable supercapacitors, J. Power Sources 854 (2021), https://doi.org/10.1016/j.jallcom.2020.157289.

[14] A. Ermolieff, M. Girard, C. Raoul, C. Bertrand, T.M. Duc, An XPS comparative study on thermal oxide barrier formation on Nb and NbN thin films, Appl. Surf. Sci. 21 (1985) 65–79, https://doi.org/10.1016/0378-5963(85)90008-X.

[15] N.R. Reddy, M.M. Kumari, M.V. Shankar, K.R. Reddy, S.W. Joo, T.M. Aminabhavi, Photocatalytic hydrogen production from dye contaminated water and electrochemical supercapacitors using carbon nanohorns and TiO2 nanoflower heterogeneous catalysts, J. Environ. Manage. 277 (2021), https://doi.org/10.1016/j.jenvman.2020.111433.

[16] W. Wang, S. Guo, I. Lee, K. Ahmed, J. Zhong, Z. Favors, F. Zaera, M. Ozkan, C.S. Ozkan, Hydrous ruthenium oxide nanoparticles anchored to graphene and carbon nanotube hybrid foam for supercapacitors, Sci. Rep. 4 (2014) 4452–4452. http://doi.org/10.1038/srep04452.

[17] C. Sengottaiyan, R. Jayavel, R.G. Shrestha, T. Subramani, S. Maji, J.H. Kim, J.P. Hill, K. Ariga, L.K. Shrestha, Indium Oxide/Carbon Nanotube/Reduced Graphene Oxide Ternary Nanocomposite with Enhanced Electrochemical Supercapacitance, B. Chem. Soc. Jpn. 92 (2018) 521–528, https://doi.org/10.1246/bcsj.20180338.

[18] J.H. Sung, J.H. Park, D.S. Jeon, D. Kim, M.J. Yu, A.C. Khot, T.D. Dongale, T.G. Kim, Retention enhancement through capacitance-dependent voltage division analysis in 3D stackable TaOx/HfO2-based selectorless memristor, Mater. Des. 207 (2021), https://doi.org/10.1016/j.matdes.2021.109845 109845.

[19] Y. Wei, N. Zhang, C. Jin, J. Shen, J. Xie, Z. Dai, L. Hu, Y. Zeng, Z. Jian, A Bi1/2K1/2TiO3-based ergodic relaxor ceramic for temperature-stable energy storage applications, Mater. Des. 207 (2021), https://doi.org/10.1016/j.matdes.2021.109887 109887.

[20] W.R. Cai, R.K. Kankala, M.T. Xiao, N. Zhang, X.Q. Zhang, Three-dimensional hollow N-doped ZIF-8-derived carbon@MnO2 composites for supercapacitors, Appl. Surf. Sci. 528 (2020), https://doi.org/10.1016/j.apsusc.2020.146921.

[21] Y. Ding, Y.C. Li, Y.J. Dai, X.H. Han, B. Xing, L.J. Zhu, K.Z. Qiu, S.R. Wang, A novel approach for preparing in-situ nitrogen doped carbon via pyrolysis of bean pulp for supercapacitors, Energy 216 (2021), https://doi.org/10.1016/j.energy.2020.119227.

[22] Y. Liang, Y.H. Lu, G.Y. Xiao, J.H. Zhang, H.J. Chi, Y. Dong, Hierarchical porous nitrogen-doped carbon microspheres after thermal rearrangement as high performance electrode materials for supercapacitors, Appl. Surf. Sci. 529 (2020), https://doi.org/10.1016/j.apsusc.2020.147141.

[23] J.H. Zhang, H. Chen, J.B. Bai, M. Xu, C.L. Luo, L.X. Yang, L.J. Bai, D.L. Wei, W.X. Wang, H.W. Yang, N-doped hierarchically porous carbon derived from grape marcs for high-performance supercapacitors, J. Power Sources 854 (2021), https://doi.org/10.1016/j.jallcom.2020.157207.

[24] Z.H. Pan, X.H. Ji, Facile synthesis of nitrogen and oxygen co-doped C@Ti3C2 MXene for high performance symmetric supercapacitors, J. Power Sources 439 (2019), https://doi.org/10.1016/j.jpowsour.2019.227068.

[25] S.Q. Wu, D.H. Wei, Y.B. Yin, Q.Q. Li, H.S. Wang, W.T. Chen, Y.F. Jiang, X.Q. Tao, N, S co-doped activated carbon with porous architecture derived from partial poly (2, 2 '-dithiodianiline) for supercapacitors, J. Energy Storage 33 (2021), https://doi.org/10.1016/j.est.2020.102043.

[26] G.F. Zheng, Z.C. Huang, Z. Liu, Cooperative utilization of beet pulp and industrial waste fly ash to produce N/P/O self-co-doped hierarchically porous carbons for high-performance supercapacitors, J. Power Sources 482 (2021), https://doi.org/10.1016/j.jpowsour.2020.228935.

[27] Y. Feng, S. Chen, J. Wang, B. Lu, Carbon foam with microporous structure for high performance symmetric potassium dual-ion capacitor, J. Energy Chem. 43 (2020) 129–138, https://doi.org/10.1016/j.jechem.2019.08.013.

[28] X.H. Xia, Y.Q. Zhang, D.L. Chao, Q.Q. Xiong, Z.X. Fan, X.L. Tong, J.P. Tu, H. Zhang, H.J. Fan, Tubular TiC fibre nanostructures as supercapacitor electrode materials with stable cycling life and wide-temperature performance, Energy Environ. Sci. 8 (2015) 1559–1568, https://doi.org/10.1039/c5ee00339c.

[29] J. Feng, X. Sun, C.Z. Wu, L.L. Peng, C.W. Lin, S.L. Hu, J.L. Yang, Y. Xie, Metallic Few-Layered VS2 Ultrathin Nanosheets: High Two-Dimensional Conductivity for In-Plane Supercapacitors, J. Am. Chem. Soc. 133 (2011) 17832–17838, https://doi.org/10.1021/ja207176c.

[30] B. Wei, H. Liang, D. Zhang, Z. Qi, H. Shen, Z. Wang, Magnetron sputtered TiN thin films toward enhanced performance supercapacitor electrodes, Mater. Renew. Sustain. Energy 7 (2018) 11, https://doi.org/10.1007/s40243-018-0117-9.

[31] C.N.R. Rao, K. Pramoda, Borocarbonitrides, BxCyNz, 2D Nanocomposites with Novel Properties, B. Chem. Soc. Jpn. 92 (2019) 441–468, https://doi.org/10.1246/bcsj.20180335.

[32] J. Shi, B.L. Jiang, C. Li, F.Y. Yan, D. Wang, C. Yang, J.J. Wan, Review of Transition Metal Nitrides and Transition Metal Nitrides/Carbon nanocomposites for supercapacitor electrodes, Mater. Chem. Phys. 245 (2020), https://doi.org/10.1016/j.matchemphys.2019.122533.

[33] Z. Qi, B. Wei, J. Wang, Y. Yang, Z. Wang, Nanostructured porous CrN thin films by oblique angle magnetron sputtering for symmetric supercapacitors, J. Power Sources 806 (2019) 953–959, https://doi.org/10.1016/j.jallcom.2019.07.325.

[34] B. Wei, H. Liang, D. Zhang, Z. Wu, Z. Qi, Z. Wang, CrN thin films prepared by reactive DC magnetron sputtering for symmetric supercapacitors, J. Mater. Chem. A 5 (2017) 2844–2851, https://doi.org/10.1039/c6ta09985h.

[35] E. Haye, A. Achour, A. Guerra, F. Moulaï, T. Hadjersi, R. Boukherroub, A. Panepinto, T. Brousse, J.-J. Pireaux, S. Lucas, Achieving on chip micro-supercapacitors based on CrN deposited by bipolar magnetron sputtering at glancing angle, Electrochim. Acta 324 (2019), https://doi.org/10.1016/j.electacta.2019.134890 134890.

[36] A. Achour, R.L. Porto, M.-A. Soussou, M. Islam, M. Boujtita, K.A. Aissa, L. Le Brizoual, A. Djouadi, T. Brousse, Titanium nitride films for micro-supercapacitors: Effect of surface chemistry and film morphology on the capacitance, J. Power Sources 300 (2015) 525–532, https://doi.org/10.1016/j.jpowsour.2015.09.012.

[37] X. Lu, G. Wang, T. Zhai, M. Yu, S. Xie, Y. Ling, C. Liang, Y. Tong, Y. Li, Stabilized TiN Nanowire Arrays for High-Performance and Flexible Supercapacitors, Nano Lett. 12 (2012) 5376–5381, https://doi.org/10.1021/nl302761z.

[38] R. Lucio-Porto, S. Bouhtiyya, J.F. Pierson, A. Morel, F. Capon, P. Boulet, T. Brousse, VN thin films as electrode materials for electrochemical capacitors, Electrochim. Acta 141 (2014) 203–211, https://doi.org/10.1016/j.electacta.2014.07.056.

[39] K. Robert, C. Douard, A. Demortière, F. Blanchard, P. Roussel, T. Brousse, C. Lethien, On Chip Interdigitated Micro-Supercapacitors Based on Sputtered Bifunctional Vanadium Nitride Thin Films with Finely Tuned Inter- and Intracolumnar Porosities, Adv. Mater. Technol. 3 (2018) 1800036, https://doi.org/10.1002/admt.201800036.

[40] G. Ma, Z. Wang, B. Gao, T. Ding, Q. Zhong, X. Peng, J. Su, B. Hu, L. Yuan, P.K. Chu, J. Zhou, K. Huo, Multilayered paper-like electrodes composed of alternating stacked mesoporous Mo2N nanobelts and reduced graphene oxide for flexible all-solid-state supercapacitors, J. Mater. Chem. A 3 (2015) 14617–14624, https://doi.org/10.1039/C5TA02851E.

[41] L. Chen, C. Liu, Z. Zhang, Novel (111) oriented γ-Mo$_2$N thin films deposited by magnetron sputtering as an anode for aqueous micro-supercapacitors, Electrochim. Acta 245 (2017) 237–248, https://doi.org/10.1016/j.electacta.2017.05.102.

[42] F.F. Klimashin, H. Euchner, P.H. Mayrhofer, Computational and experimental studies on structure and mechanical properties of Mo-Al-N, Acta Mater. 107 (2016) 273–278, https://doi.org/10.1016/j.actamat.2016.01.063.

[43] B.B. Wei, F.W. Ming, H.F. Liang, Z.B. Qi, W.S. Hu, Z.C. Wang, All nitride asymmetric supercapacitors of niobium titanium nitride-vanadium nitride, J. Power Sources 481 (2021), https://doi.org/10.1016/j.jpowsour.2020.228842.

[44] B. Peng, H.Q. Li, Q. Zhang, Y.X. Xu, T.F. Wei, Q.M. Wang, F.G. Zhang, K.H. Kim, High-temperature thermal stability and oxidation resistance of Cr and Ta co-alloyed Ti - Al - N coatings deposited by cathodic arc evaporation, Corrosion Science 167 (2020), https://doi.org/10.1016/j.corsci.2020.108490.

[45] O. Ostrovskaya, C. Badini, S.M. Deambrosis, E. Miorin, S. Biamino, E. Padovano, Protection from oxidation of second and third generation TiAl intermetallic alloys by magnetron sputtering deposition of a TiAl/TiAlN coating, Mater. Des. 208 (2021), https://doi.org/10.1016/j.matdes.2021.109905 109905.

[46] Z. Gao, Z. Wu, S. Zhao, T. Zhang, Q. Wang, Enhanced capacitive property of HfN film electrode by plasma etching for supercapacitors, Materials Letters 235 (2019) 148–152, https://doi.org/10.1016/j.matlet.2018.10.032.

[47] B. Wei, G. Mei, H. Liang, Z. Qi, D. Zhang, H. Shen, Z. Wang, Porous CrN thin films by selectively etching CrCuN for symmetric supercapacitors, J. Power Sources 385 (2018) 39–44, https://doi.org/10.1016/j.jpowsour.2018.03.023.

[48] Y.J. Kim, T.J. Byun, H.Y. Lee, J.G. Han, Effect of bilayer period on CrN/Cu nanoscale multilayer thin films, Surf. Coat. Technol. 202 (2008) 5508–5511, https://doi.org/10.1016/j.surfcoat.2008.06.028.

[49] J. Musil, P. Zeman, H. Hruby, P.H. Mayrhofer, ZrN/Cu nanocomposite film - a novel superhard material, Surf. Coat. Technol. 120 (1999) 179–183, https://doi.org/10.1016/S0257-8972(99)00482-X.

[50] P. Zeman, R. Cerstvy, P.H. Mayrhofer, C. Mitterer, J. Musil, Structure and properties of hard and superhard Zr-Cu-N nanocomposite coatings, Mater. Sci. Eng. Struct. Mater. Properties Microstruct. Process. 289 (2000) 189–197, https://doi.org/10.1016/s0921-5093(00)00917-5.

[51] J. Musil, H. Hruby, P. Zeman, H. Zeman, R. Cerstvy, P.H. Mayrhofer, C. Mitterer, Hard and superhard nanocomposite Al-Cu-N films prepared by magnetron sputtering, Surf. Coat. Technol. 142 (2001) 603–609, https://doi.org/10.1016/S0257-8972(01)01200-2.

[52] H. Zeman, J. Musil, J. Vlcek, P.H. Mayrhofer, C. Mitterer, Thermal annealing of sputtered Al-Si-Cu-N films, Vacuum 72 (2003) 21–28, https://doi.org/10.1016/S0042-207x(03)00094-0.

[53] A. Akbari, C. Templier, M.F. Beaufort, D. Eyidi, J.P. Riviere, Ion beam assisted deposition of TiN–Ni nanocomposite coatings, Surf. Coat. Technol. 206 (2011) 972–975, https://doi.org/10.1016/j.surfcoat.2011.03.102.

[54] Z.R. Liu, Y.X. Xu, B. Peng, W. Wei, L. Chen, Q.M. Wang, Structure and property optimization of Ni-containing AlCrSiN coatings by nano-multilayer construction, J. Power Sources 808 (2019), https://doi.org/10.1016/j.jallcom.2019.07.342.

[55] A.V. Chernogor, F.F. Klimashin, A.O. Volkhonskii, I.V. Blinkov, P.H. Mayrhofer, The impact of Ni and Mo on growth-morphology and mechanical properties of arc evaporated Ti-Cr-N hard coatings, Surf. Coat. Technol. 377 (2019), https://doi.org/10.1016/j.surfcoat.2019.124917.

[56] C. Hu, Y.X. Xu, L. Chen, F. Pei, Y. Du, Mechanical properties, thermal stability and oxidation resistance of Ta-doped CrAlN coatings, Surf. Coat. Technol. 368 (2019) 25–32, https://doi.org/10.1016/j.surfcoat.2019.04.026.

[57] S. Calderon Velasco, A. Cavaleiro, S. Carvalho, Functional properties of ceramic-Ag nanocomposite coatings produced by magnetron sputtering, Prog. Mater. Sci. 84 (2016) 158–191, https://doi.org/10.1016/j.pmatsci.2016.09.005.

[58] S.M. Aouadi, D.P. Singh, D.S. Stone, K. Polychronopoulou, F. Nahif, C. Rebholz, C. Muratore, A.A. Voevodin, Adaptive VN/Ag nanocomposite coatings with lubricious behavior from 25 to 1000°C, Acta Mater. 58 (2010) 5326–5331, https://doi.org/10.1016/j.actamat.2010.06.006.

[59] H. Li, C. Zhang, C. Liu, M. Huang, Improvement in corrosion resistance of CrN coatings, Surf. Coat. Technol. (2018), https://doi.org/10.1016/j.surfcoat.2018.07.018.

[60] P.H. Mayrhofer, G. Tischler, C. Mitterer, Microstructure and mechanical/thermal properties of Cr–N coatings deposited by reactive unbalanced magnetron sputtering, Surf. Coat. Technol. 142–144 (2001) 78–84, https://doi.org/10.1016/S0257-8972(01)01090-8.

[61] J.-Z. Kong, C. Li, X.-Y. Sun, Y. Xuan, H.-F. Zhai, A.-D. Li, Q.-Z. Wang, F. Zhou, Improved tribological properties and corrosion protection of CrN coating by ultrathin composite oxide interlayer, Appl. Surf. Sci. 541 (2021), https://doi.org/10.1016/j.apsusc.2020.148606 148606.

[62] P.H. Mayrhofer, H. Willmann, C. Mitterer, Oxidation kinetics of sputtered Cr-N hard coatings, Surf. Coat. Technol. 146 (2001) 222–228, https://doi.org/10.1016/s0257-8972(01)01471-2.

[63] J. Jin, D. Zheng, S. Han, J. Ma, Z. Zhu, Effect of Ni content on the electrical and corrosion properties of CrNiN coating in simulated proton exchange membrane fuel cell, Int. J. Hydrogen. Energ 42 (2017) 1142–1153, https://doi.org/10.1016/j.ijhydene.2016.11.007.

[64] A. Ruden, E. Restrepo-Parra, A.U. Paladines, F. Sequeda, Corrosion resistance of CrN thin films produced by dc magnetron sputtering, Appl. Surf. Sci. 270 (2013) 150–156, https://doi.org/10.1016/j.apsusc.2012.12.148.

[65] J. Huang, B.G. Sumpter, V. Meunier, A Universal Model for Nanoporous Carbon Supercapacitors Applicable to Diverse Pore Regimes, Carbon Materials, and Electrolytes,, Chem. AEuropean J. 14 (2008) 6614–6626, https://doi.org/10.1002/chem.200800639.

[66] P.C. Wo, P.R. Munroe, Z.-T. Jiang, Z. Zhou, K.Y. Li, Z. Xie, Enhancing toughness of CrN coatings by Ni addition for safety-critical applications, Mater. Sci. Eng. A 596 (2014) 264–274, https://doi.org/10.1016/j.msea.2013.12.064.

[67] W.L. Cheng, Z.F. Zhou, P.W. Shum, K.Y. Li, Effect of Ni addition on the structure and properties of Cr–Ni–N coatings deposited by closed-field unbalanced magnetron sputtering ion plating, Surf. Coat. Technol. 229 (2013) 84–89, https://doi.org/10.1016/j.surfcoat.2012.12.032.

[68] H. Cui, G. Zhu, X. Liu, F. Liu, Y. Xie, C. Yang, T. Lin, H. Gu, F. Huang, Niobium nitride Nb_4N_5 as a new high-performance electrode material for supercapacitors, Adv. Sci. 2 (2015) 1500126, https://doi.org/10.1002/advs.201500126.

[69] L. Wang, H. Ji, S. Wang, L. Kong, X. Jiang, G. Yang, Preparation of Fe_3O_4 with high specific surface area and improved capacitance as a supercapacitor, Nanoscale 5 (2013) 3793–3799, https://doi.org/10.1039/C3NR00256J.

[70] Y. Xie, D. Wang, Supercapacitance performance of polypyrrole/titanium nitride/polyaniline coaxial nanotube hybrid, J. Power Sources 665 (2016) 323–332, https://doi.org/10.1016/j.jallcom.2016.01.089.

[71] Y. Wang, M. Jiang, Y. Yang, F. Ran, Hybrid electrode material of vanadium nitride and carbon fiber with cigarette butt/metal ions wastes as the precursor for supercapacitors, Electrochimica Acta 222 (2016) 1914–1921, https://doi.org/10.1016/j.electacta.2016.12.003.

[72] A. Achour, M. Chaker, H. Achour, A. Arman, M. Islam, M. Mardani, M. Boujtita, L. Le Brizoual, M.A. Djouadi, T. Brousse, Role of nitrogen doping at the surface of titanium nitride thin films towards capacitive charge storage enhancement, J. Power Sources 359 (2017) 349–354, https://doi.org/10.1016/j.jpowsour.2017.05.074.